



Hybridization of graphene oxide with commercial graphene for constructing 3D metal-free aerogel with enhanced photocatalysis

Kang-Qiang Lu^{a,b}, Lan Yuan^{a,b}, Xin Xin^{a,b}, Yi-Jun Xu^{a,b,*}

^a State Key Laboratory of Photocatalysis on Energy and Environment, College of Chemistry, Fuzhou University, Fuzhou, 350116, PR China

^b College of Chemistry, New Campus, Fuzhou University, Fuzhou, 350116, PR China



ARTICLE INFO

Keywords:

Electrical conductivity
Aerogel
Graphene oxide
Commercial elicarb graphene
Photocatalysis

ABSTRACT

The electrical conductivity and charge carrier mobility of reduced graphene oxide (RGO) based 3D aerogel using graphene oxide (GO) as precursor is often restricted by the intrinsic population of defects and thus disruption of 2D π -conjugation in the domain of RGO sheets. Here, we report a facile and efficient approach to improve the electrical conductivity of RGO aerogel by introducing highly conductive commercial Elicarb graphene (EGR). GO acting as a “macromolecular surfactant” can be used to simultaneously resolve the intrinsic drawback of low solution dispersibility of EGR and provides the basic skeleton for solution-processable synthesis of RGO@EGR-Eosin Y (RGO@EGR-EY) metal-free 3D aerogel composites. The as-synthesized RGO@EGR-EY aerogel with superior electrical conductivity facilitates more efficient separation and transfer of photogenerated charge carriers, and consequently exhibits much higher photocatalytic activity than RGO-EY aerogel. It is hoped that our current work could open promising prospects for the rational utilization of highly conductive commercial graphene to fabricate graphene-based aerogel for enhanced photoredox applications.

1. Introduction

Three-dimensional (3D) graphene-based aerogel, by virtue of its many interesting physicochemical properties, has proved itself as an exciting monolith material for constructing high-efficiency photocatalyst for practical applications of solar energy conversion [1–6]. Such a 3D porous monolith structure can afford the large accessible surface area, easy recyclability and efficient light harvesting ability due to the multi-reflection within interconnected open-framework, which benefits for facilitated adsorption and photoreaction [7–9]. Moreover, 3D porous structure of aerogel can substantially inhibit the aggregation or stacking of subunits, thus exposing more active sites for catalytic surface reaction [10,11]. Regarding the synthesis of graphene aerogel-based photocatalysts, graphene oxide (GO), owing to its amenable and flexible solution processability is often adopted as the precursor of graphene aerogel. Under hydrothermal treatment or in the presence of reducing agents, GO can be reduced to graphene and in situ self-assembled into a 3D architecture with the $\pi-\pi$ stacking and hydrogen bonds between nanosheets [9,12]. However, the electrical conductivity and charge carrier mobility of reduced GO (RGO) aerogel is remarkably decreased, which is because the large population of defects of RGO results in considerable disruption of the 2D π -conjugation in the domain of RGO sheets [13,14]. And this in turn results in the fact that the net

improvement efficiency of RGO aerogel-based photoactivity is often restricted [15–17]. Therefore, one important strategy for enhancing the photocatalytic performance of RGO aerogel-based photocatalyst is to improve the electronic conductivity of the cross-linked 3D framework composed of RGO sheets by the use of selective viable approaches.

Commercial Elicarb graphene (EGR), which is manufactured on a large scale via a high-shear exfoliation process in liquid phase, has attracted great attention in recent years [18,19]. Being different from the oxidation-exfoliation-reduction approach, the high-shear exfoliation process includes neither the strong oxidation of graphite nor the subsequent reduction process, which results in the EGR possessing less structural defects and superior electrical conductivity [20,21]. Therefore, coupling the highly conductive commercial EGR with RGO aerogel could be a feasible approach to improve the electronic conductivity of 3D framework of RGO aerogel. However, owing to the intrinsic hydrophobic nature of EGR, the direct dispersion of EGR in water has been generally considered unattainable [22]. To process EGR in benign solvents, the surfaces of EGR have to be modified either covalently with solvent-like functional groups or by coating with surfactant or solvent-like polymers [23–25]. However, a fundamental tradeoff of such strategy is that it tends to sacrifice the intrinsic material properties of EGR for enhanced processability. Surface coating usually introduces hard-to-remove and insulating surfactants or polymers, while covalent

* Corresponding author at: State Key Laboratory of Photocatalysis on Energy and Environment, College of Chemistry, Fuzhou University, Fuzhou, 350116, PR China.
E-mail address: yjxu@fzu.edu.cn (Y.-J. Xu).

functional groups inevitably break the π -conjugated carbon surfaces [26–28].

Notably, apart from the role as the precursor to make graphene, Huang's group recently has highlighted the new multifaces of GO as "a big macromolecular surfactant" to disperse insoluble materials such as graphite and carbon nanotubes [14,29–32]. The oxygen-containing groups render GO sheets hydrophilic and highly dispersible in water, whereas the aromatic regions offer active sites to interact with the graphite and carbon nanotubes through π - π supramolecular interactions [26,33]. Therefore, it will be a feasible approach to disperse EGR in solution phase by using GO as the surfactant, and this approach can realize the purpose of killing two birds with one stone. On the one hand, the utilization of GO as a dispersing agent can generate a clean, electrically addressable carbon–carbon interfaces in the final composite because GO can be cleanly converted to RGO without producing hard-to-remove byproducts. On the other hand, GO can provide a basic skeleton to directly construct the EGR doped RGO (RGO@EGR) aerogel composites.

Against this background, we herein report the rational synthesis of a series of metal-free EGR doped RGO-Eosin Y aerogel (RGO@EGR-EY aerogel) photocatalysts with different weight addition ratios of EGR, during which GO acting as surfactant has been used to disperse EGR in the wet-chemistry synthesis process. The as-obtained RGO@EGR-EY aerogels possess the robust characteristics of 3D monolith, but exhibit the distinctly improved electrical conductivities as compared to RGO aerogels. The photoactivity assay under identical reaction conditions highlights that the RGO@EGR-EY aerogels exhibit much higher visible light activity than RGO-EY aerogel. It is expected that this work could open up new frontiers for improving the electrical conductivity of the 3D framework of RGO aerogel by utilizing commercial, highly conductive graphene and constructing more efficient aerogel-based photocatalyst for artificial redox catalysis.

2. Experimental

2.1. Materials

Hydrochloric acid (HCl), concentrated sulfuric acid (H_2SO_4 , 98%), potassium permanganate ($KMnO_4$), hydrogen peroxide (H_2O_2 , 30%), Eosin Y (EY) were all obtained from Sinopharm Chemical Reagent Co., Ltd. (Shanghai, China). Graphite powder was supplied by Qingdao Zhongtian Company, China. Elicarb graphene (EGR) was obtained from Thomas Swan Co. Ltd. (UK). All reagents were used as received without further purification. The deionized (DI) water used in the experiment was from local sources.

2.2. Preparation of graphene oxide and RGO-EY aerogels

Graphene oxide (GO) was synthesized from natural graphite powder by a modified Hummers method [34–37]. The preparation of RGO-EY aerogels was based on a facile one-step hydrothermal method. The primary difference of synthesis protocols from previous work [38] was that the hydrothermal treatment temperature in this work was 180 °C because it can yield the more mechanically robust 3D aerogels. The details are presented in the Supporting Information.

2.3. Preparation of RGO@EGR-EY aerogels

The preparation process of RGO@EGR-EY aerogels is illustrated in Scheme 1. EGR was dispersed using GO as surfactant with the assist of ultrasound. Typically, the given amount of EGR was added into 10 mL deionized water, and the resulting mixture was sonicated for 0.5 h to form a uniform dispersion. Then, a certain amount of GO suspension was added into the EGR dispersion and sonicated for 4 h to form a uniform GO@EGR dispersion. The total mass of GO@EGR was maintained at 30 mg. After that, 4 mL of the EY aqueous (0.5 mg/mL)

solution was added into the above mixtures. DI water was added into the above mixtures to a volume of 30 mL. After being stirred for 6 h, the mixture was transferred into a 50 mL Teflon-lined autoclave and subjected to hydrothermal treatment at 180 °C for 12 h. The as-prepared RGO@EGR-EY hydrogels were taken out with tweezers, washed several times with deionized water, and treated by freeze-drying. Finally, the RGO@EGR-EY aerogels with different weight ratios of EGR (5%, 10%, 15%, 20%) were obtained. For the comparison purpose, the RGO@EGR aerogel was also synthesized via the same procedure without the addition of EY.

2.4. Characterization

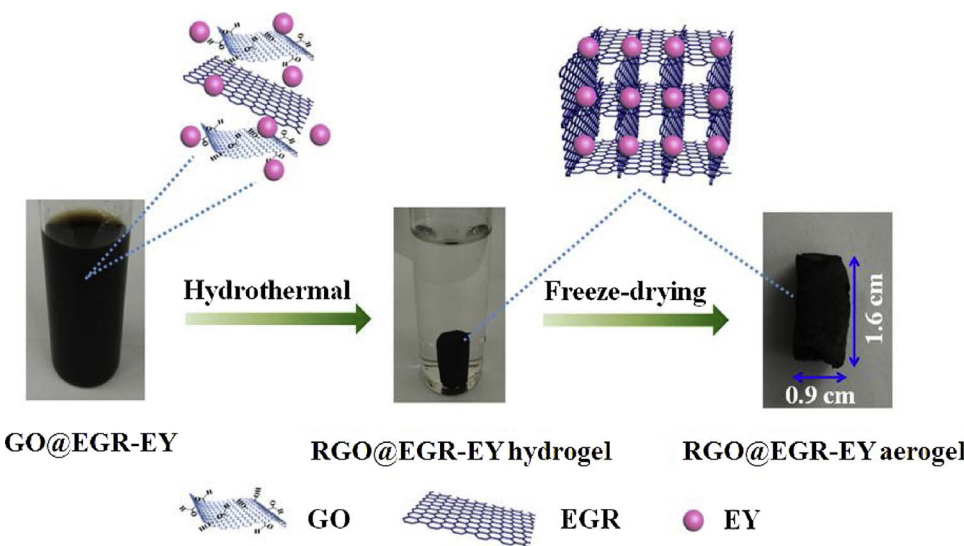
X-ray photoelectron spectroscopy (XPS) analysis was completed on a Thermo Scientific ESCA Lab 250 spectrometer equipped with a mono chromatic Al K α (X-ray source), a multiaxial sample stage and a hemispherical analyzer. The calibration of the binding energies was based on the C 1s peak at 284.6 eV. A Nanoscope IIIA system was used to measure the atomic force microscopy (AFM) spectra. Scanning electron microscopy (SEM, FEI Nova NANOSEM 230) and transmission electron microscopy (TEM, FEI Tecnai G2 F20 S-TWIN) were used to determine the morphology and microscopic structure of the samples. The electrical conductivity measurement of graphene (RGO and EGR) was performed by measuring the resistivity-pressure curve (R-P curve) using a four-point probe technique on a ST2722 (Suzhou Jingge Electronic Co., P. R. China) power resistivity tester. A Renishaw inVia Raman System 1000 with a 532 nm Nd:YAG excitation source was employed to collect the Raman spectra at room temperature. The nitrogen adsorption-desorption isotherms and Brunauer-Emmett-Teller (BET) surface areas were measured on a Micromeritics ASAP2010 equipment. The photoluminescence (PL) spectra were obtained using an Edinburgh Analytical Instrument PLS920 system. The contact angle of the prepared membranes was analyzed using a contact angle goniometer (OCA-20, Dataphysics, Germany).

Photoelectrochemical measurements were performed in a homemade three electrode quartz cell with a PAR VMP3 Multi Potentiostat apparatus. A Pt plate was used as the counter electrode, and Ag/AgCl electrode was used as the reference electrode. The working electrode was prepared on fluorine-doped tin oxide (FTO) glass that was cleaned by ultrasonication in ethanol for 30 min and dried at 80 °C. Typically, 5 mg of the sample powder was ultrasonicated in 0.5 mL of ethanol to disperse it evenly to get a slurry. The slurry was spread onto FTO glass, whose side part was previously protected using Scotch tape. After air drying, the working electrode was further dried at 100 °C for 2 h to improve adhesion. Then, the Scotch tape was unstuck, and the uncoated part of the electrode was isolated with epoxy resin. The exposed area of the working electrode was 0.25 cm². The electrochemical impedance spectroscopy (EIS) measurement and cyclic voltammograms were carried out using a CHI-660D workstation, (CH Instrument, USA) in the three electrode cell in the presence of 0.5 M KCl solution containing 0.01 mM $K_3[Fe(CN)_6]/K_4[Fe(CN)_6]$ (1:1) under open circuit potential conditions. The photocurrent measurement was carried out on a BAS Epsilon workstation without bias and the electrolyte was 0.2 M aqueous Na_2SO_4 solution (pH = 6.8) without an additive. The visible light irradiation source was a 300 W Xe arc lamp system equipped with a UV-CUT filter ($\lambda > 420$ nm).

2.5. Photocatalytic reduction of Cr(VI)

The photocatalytic reduction of Cr(VI) over the as-synthesized graphene-organics aerogels was performed in an aqueous solution under the irradiation of visible light. A graphene-EY aerogel sample and 60 μ L of triethanolamine (TEOA, sacrificial agent) were added into 50 mL of 20 mg L⁻¹ aqueous solution of Cr(VI) in a quartz vial. Prior to irradiation, the above suspension was kept in the dark for 1 h to establish adsorption-desorption equilibrium between the photocatalyst

Scheme 1. Schematic illustrations of the preparation of RGO@EGR-EY hydrogel and aerogel.



and the reactant, followed by irradiation with a 300 W Xe arclamp (PLS-SXE 300C, Beijing Perfectlight Co., Ltd.) equipped with a filter to cut off light of wavelength below 420 nm ($\lambda > 420$ nm), and the intensity of visible light irradiation was about 0.6 W cm^{-2} . During the reaction process, 3 mL of sample solution was collected at a certain time interval and analyzed on a Varian ultraviolet-visible light (UV-vis) spectrophotometer (Cary-50, Varian Co.). The whole experimental process was conducted under N_2 bubbling at a flow rate of 60 mL min^{-1} . The percentage of reduction of Cr(VI) is reported as C/C_0 . Here, C is the concentration of Cr(VI) solution at each irradiated time interval, while C_0 is the initial concentration of Cr(VI) before visible light irradiation. The recycling test of the synthesized aerogel catalyst was done as follows. Typically, when a photocatalytic cycle was finished, the aerogel catalyst was separated from the reaction solution using tweezers, rinsed, and then directly employed in the next photocatalytic cycle. Between the two cycles, it is unnecessary to perform tedious and sophisticated centrifugation/filtration, sonication, and drying processes.

3. Results and discussion

There are two obvious structural differences between graphene oxide (GO) prepared by modified Hummers' method [34,35,37] and commercial Elicarb graphene (EGR) that is manufactured *via* a high-shear exfoliation process in liquid phase [19,20]. One is that the defects density of EGR is distinctly lower than that of GO, as evidenced by Raman spectra. As can be seen clearly in Fig. 1A, the I_D/I_G ratio is 0.14 for EGR, which is remarkably lower than 1.01 for GO, indicating the much lower defects density of EGR than that of GO [14,16,39]. The other structural feature is that, for EGR, the amount of surface oxygenated functional groups is significantly lower than GO, which can be reflected by the direct comparison of C 1s spectra between EGR and GO, as displayed in Fig. 1B. An abundance of oxygenated functional groups on GO sheets make it act as "a big macromolecular surfactant" well dispersed in an aqueous phase [35,40]. As shown in Fig. 1C, the colloidal dispersion of GO has been found to be stable for at least months. However, after sonication, the majority of EGR powder contains coagulated architectures at the bottom of vial due to its hydrophobic property. In order to resolve the low solution dispersibility deficiency of EGR, GO acting as surfactant has been used to disperse EGR. According to recent studies [13,29], GO sheet consists of two types of randomly distributed regions: aromatic regions with unoxidized benzene rings and regions with aliphatic six-membered rings. Such a special molecular structure makes GO behave like an amphiphilic molecule and

allows the formation of Langmuir–Blodgett films on a water surface in the absence of other amphiphilic molecules [30,31,41,42]. The oxygen-containing groups render GO sheets hydrophilic and highly dispersible in water, whereas the aromatic regions offer active sites to interact with EGR through π - π supramolecular interactions [26]. Therefore, the excellent water processability of GO could be inherited by forming complexes with EGR, which favors the assembly of RGO@EGR-EY aerogel [3,8]. As shown in Fig. 1C, when the yellow color aqueous colloidal suspension of GO is mixed with EGR, the GO@EGR suspension turns black and remains stable even after two months deposition. Furthermore, the hydrophilicity of the samples has also been investigated by water contact angle measurement. Lower contact angle indicates that the membrane surface is more hydrophilic in nature [43,44]. As shown in Fig. S1, while a big contact angle of 74.5° is observable for the EGR membrane, the GO@EGR membrane shows a much smaller contact angle of 47.6° , indicating the fact that GO can act as surfactant to disperse EGR effectively.

The four-point probe technique has been employed to investigate the electrical conductivity of graphene (EGR and RGO). As shown in Fig. 1D, under the pressure range of 2–20 MPa, the resistivity-pressure (R-P) curves of the EGR and RGO samples show that the resistivity of EGR is much lower than that of RGO. Since that the electrical conductivity is the inverse of resistivity ($1/R$), the result clearly demonstrates that the electrical conductivity of EGR is obviously much higher than that of RGO [45]. Furthermore, Fig. 1E and F displays the typical scanning electron microscopy (SEM) images of GO and EGR, respectively. It can be seen that both the GO and EGR exhibit the unique ultrathin two-dimensional structure and clean surface. The atomic force microscopy (AFM) images shown in Fig. S2 indicate that GO and EGR sheets possess the similar range of lateral size, which varies from 0.3 to $1.3 \mu\text{m}$. In addition, GO sheets exhibit an apparent thickness about 0.9 nm , which corresponds to the thickness of monolayer graphene and the thickness of EGR sheets is predominantly about 1.8 nm , corresponding to the bilayer graphene [32,46].

Fig. 2A–C shows the macroscopic appearance and SEM images of the resultant RGO-2EY aerogel and RGO@15%EGR-2EY aerogel (with optimal photocatalytic activity as examples, as discussed later). It can be seen that both the RGO-2EY aerogel and RGO@15%EGR-2EY aerogel possess the similar size with diameter of around 0.9 cm and height of approximately 1.6 cm . In addition, the SEM images of RGO-2EY aerogel and RGO@15%EGR-2EY aerogel show analogous morphologies. Both the RGO-2EY aerogels and RGO@15%EGR-2EY aerogels reveal an interconnected porous framework with random open pores constructed from the cross-linking of the graphene sheets. These

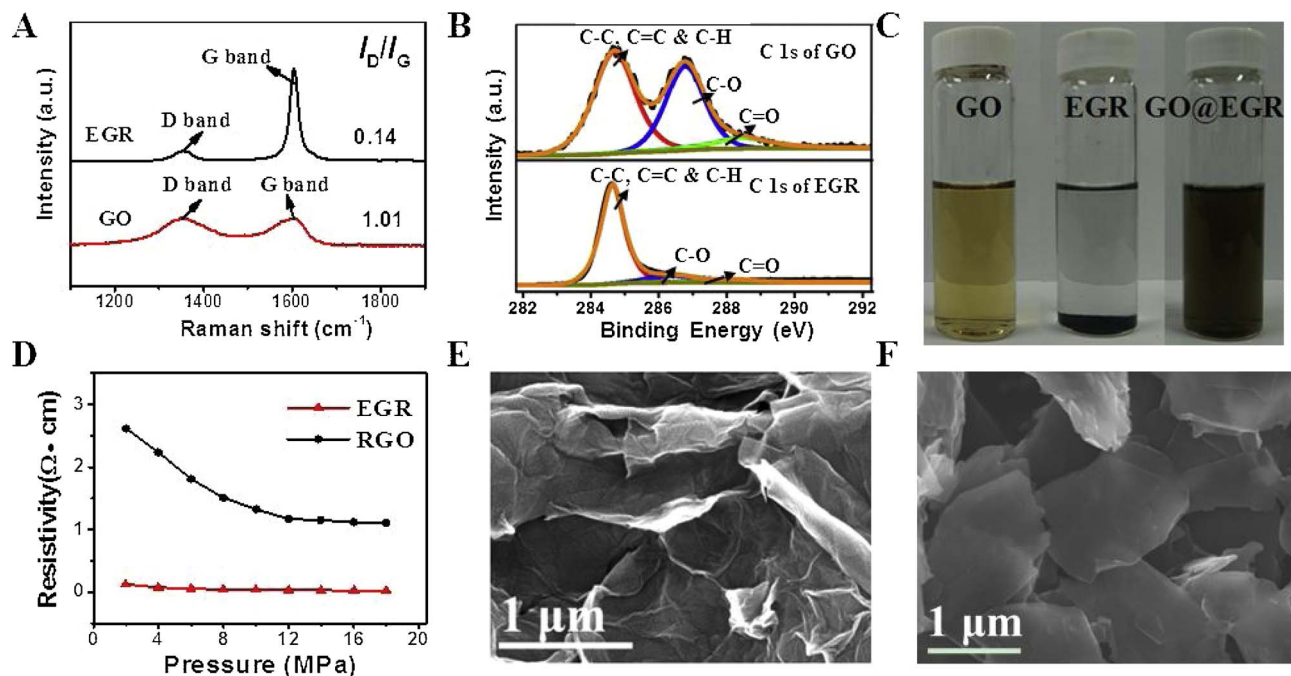


Fig. 1. Raman spectra of GO and EGR (A); XPS spectra of C 1s of GO and EGR (B); photographs of GO, EGR and GO@EGR dispersed in water (C); the resistivity-pressure (R-P) curves of EGR and RGO (D) and SEM of GO (E) and EGR (F).

results indicate that the introduction of EGR into the matrix RGO aerogel does not play a significant effect on the macroscopic appearance and microstructure construction of RGO aerogel. In addition, Fig. S3 shows the transmission electron microscopy (TEM) images of the RGO-2EY aerogel and RGO@15%EGR-2EY aerogel. It can be seen that both the RGO-2EY aerogel and RGO@15%EGR-2EY aerogel present the wrinkled sheet structure, which consists of a few layers of graphene. Notably, the introduction of EGR has not resulted in obvious aggregation in RGO@15%EGR-2EY aerogel, which is beneficial for better harnessing the electronic conductivity of graphene to promote charge carrier transportation [34,45]. The RGO-2EY aerogel and RGO@15%EGR-2EY aerogel have also been characterized by Raman spectroscopy.

As shown in Fig. 2D, the I_D/I_G ratio is 0.95 for RGO-2EY aerogel, which is lower than 1.01 for GO, indicating the enhanced graphitization of the RGO resulting from the hydrothermal reduction process [45]. Nevertheless, the I_D/I_G ratio for RGO-2EY aerogel is obviously much higher than that for RGO@15%EGR-2EY aerogel, confirming that the introduction of EGR can reduce the structure defect of RGO@EGR aerogel hybrid system. Fig. 2E displays the C 1s XPS spectra of RGO-2EY and RGO@15%EGR-2EY aerogel. In comparison with XPS spectrum of original GO in Fig. 1B, a significant loss of oxygenated functional groups is observed in RGO-2EY aerogel, which indicates the effective reduction of GO to RGO after the hydrothermal reduction treatment. However, it is notable that there still remain numerous oxygenated functional

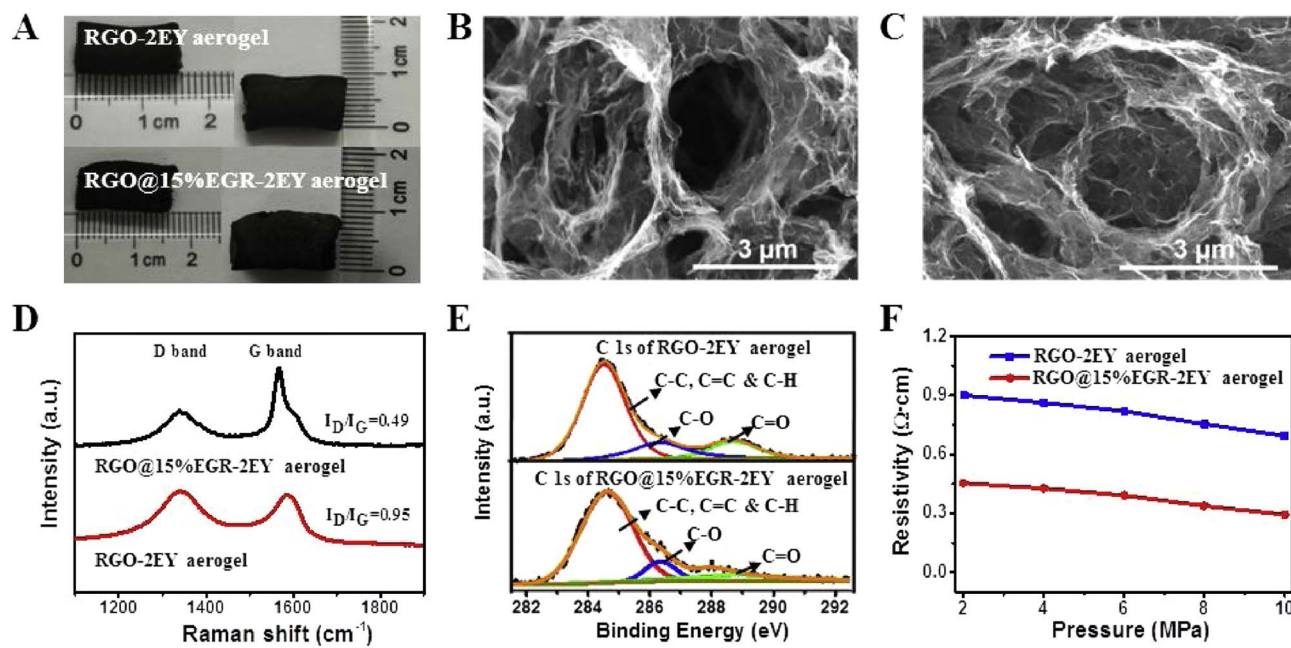


Fig. 2. Photographs of the macroscopic appearance of RGO-2EY aerogel and RGO@15%EGR-2EY aerogel (A); SEM images of RGO-2EY aerogel (B) and RGO@15%EGR-2EY aerogel (C); Raman spectra (D), XPS spectra of C 1s (E) and the resistivity-pressure (R-P) curves (F) of RGO-2EY aerogel and RGO@15%EGR-2EY aerogel.

groups in RGO-2EY aerogel, which is higher than that in RGO@15% EGR-2EY aerogel. The more residual oxygenated functional groups disrupting the long range π conjugation of RGO sheets result in the decreased conductivity of RGO-2EY as compared to that of RGO@15% EGR-2EY aerogel [16,47]. In addition, as shown in Fig. S4, the XPS study of the RGO@15%EGR-2EY aerogel reveals the peaks of Br, confirming the presence of EY in the RGO@15%EGR-2EY aerogel because Br is the typical component of EY [38]. As shown in Fig. 2F, the resistivity-pressure (R-P) curves of the RGO-2EY and RGO@15%EGR-2EY aerogel indicate that the electrical conductivity of RGO@15%EGR-2EY aerogel is obviously higher than that of RGO-2EY aerogel. Such an improved electronic conductivity of the RGO@15%EGR-2EY aerogel would benefit for the transfer process of photogenerated charge carriers across the interfacial domain between the RGO@15%EGR aerogel and EY molecule, which is generally believed to enhance the photocatalytic activity of graphene-based composite photocatalysts [2,17,48,49].

The photocatalytic activity of the graphene-EY aerogels has been evaluated by photoreduction of the carcinogenic heavy metal ion Cr (VI), which represents a promising and imperative treatment for the detoxification of electrolytic wastewaters [38,50]. As shown in Fig. S5, RGO-2EY aerogel with the addition of 2 mg EY shows the optimal photocatalytic activity toward reduction of Cr(VI). When more EY (e.g., 3 mg) is added to the GO solution during the synthesis process, the 3D architectures of RGO-EY aerogel cannot be maintained (Fig. S6). Similar result has also be observed in our previous work [38]. Therefore, the largest amount of EY in our aerogel composite photocatalysts has been determined to be 2 mg. As shown in Fig. 3A, the RGO@EGR-2EY aerogels show much higher photocatalytic activity than RGO-2EY aerogel. With the increase of EGR content in the hybrid aerogels, the RGO@EGR-2EY aerogels display progressively improved photocatalytic performance, indicating that the photoactivity of the resultant RGO@EGR-2EY aerogels is positively related to the amount of EGR in the hybrid aerogels. The optimal RGO@15%EGR-2EY aerogel can efficiently reduce 98% of Cr(VI) under visible light irradiation of 20 min. However, it is noteworthy that when more EGR (e.g., 20%) is added to

the GO solution during the synthesis process, the resulting RGO@20% EGR-2EY composite becomes soft and fragile (Fig. S7). This should be attributed to the high content of EGR resulting in the large coverage of the GO surface with EGR, which reduces the number of sites for cross linking among GO and inhibits the formation of interconnected 3D hydrogel [51]. Therefore, taking the mechanical strength and photoactivity of the resultant RGO@EGR-2EY aerogels into account, the largest weight content of EGR in the composite photocatalysts has been determined to be 15%. Furthermore, controlled experiment over the bare RGO@15%EGR aerogel and blank experiments in the absence of photocatalysts or light irradiation have been also conducted. As shown in Fig. S8, no photoactivity has been obtained in any of these cases. These results faithfully demonstrate that organic EY is the primary photoactive ingredient in the graphene-EY aerogels photocatalysts.

The stability is as important as activity for the practical application of photocatalytic materials. Taking the RGO@15%EGR-2EY aerogel as an example, we have evaluated its recyclability by 21 times, as displayed in Fig. 3B. The result shows that after about 7 h of visible light irradiation, RGO@15%EGR-2EY aerogel is able to continuously reduce Cr(VI) with only a slight photoactivity decrease. Furthermore, the strong cross-linking interaction of graphene sheets in the graphene-EY aerogels enables the 3D composite to maintain its structure after the photoactivity test, which allows the graphene-EY aerogels photocatalysts to be easily separated from a liquid reaction medium with tweezers (Fig. S9). The slight photoactivity decrease for RGO@15%EGR-2EY aerogel in the recycling process should be ascribed to the consumption of the organics EY during the photocatalytic process, which has been commonly observed in dye-sensitized photocatalyst systems [52,53]. Even so, regeneration of the photoactivity of RGO@15%EGR-2EY aerogel can be realized via a very simple rehydrothermal treatment of the used RGO@15%EGR-2EY aerogel photocatalyst with fresh EY. The three successive rehydrothermal treatment and photoactivity test in Fig. 3C clearly prove the full regeneration of the RGO@15%EGR-2EY aerogel photocatalyst after each rehydrothermal process. Therefore, it is believed that the metal-free RGO@EGR-EY aerogel holds

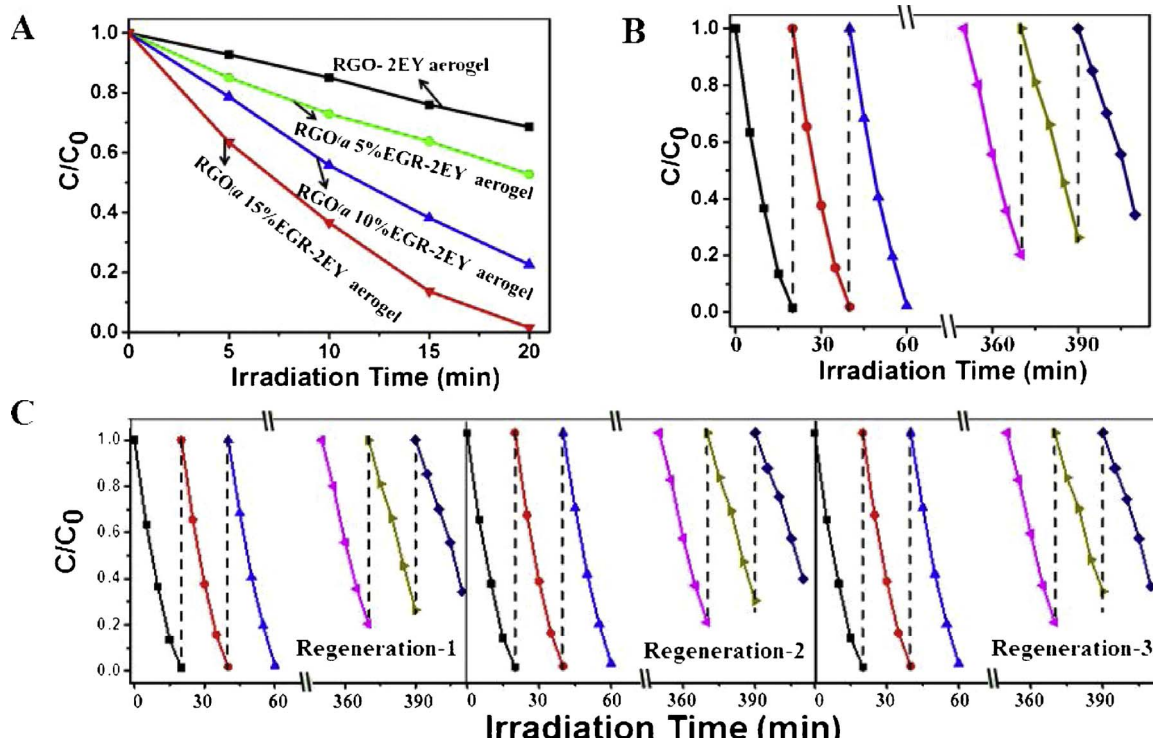


Fig. 3. Visible-light-driven ($\lambda > 420$ nm) photocatalytic reduction of Cr(VI) over RGO-2EY aerogel and RGO@EGR-2EY aerogels with different weight addition ratios of EGR (A); recycling test (B) and regeneration photoactivity test (C) of RGO@15%EGR-2EY aerogel toward the reduction of Cr(VI) under the illumination of visible light.

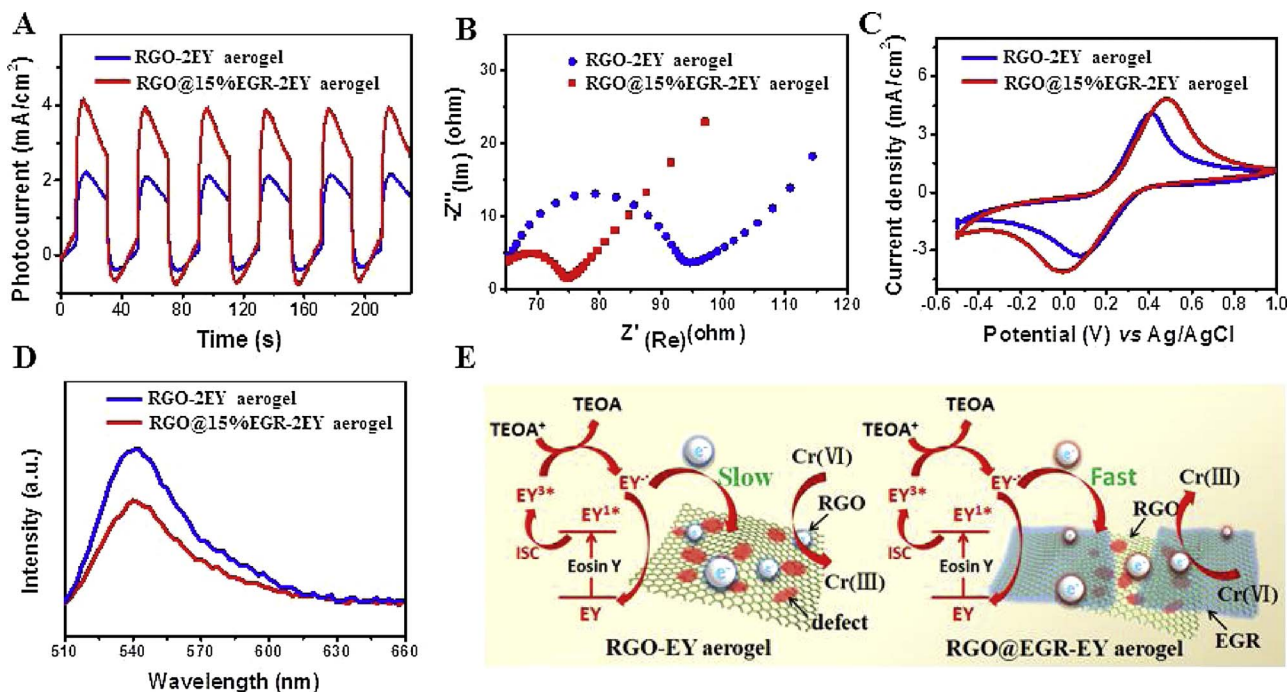


Fig. 4. Transient photocurrent responses (A); electrochemical impedance spectroscopy Nyquist plots (B); cyclic voltammograms (C) and PL spectra with an excitation wavelength of 490 nm (D) of RGO-2EY aerogel and RGO@15%EGR-2EY aerogel; schematic illustration for the photocatalytic reduction of Cr(VI) over RGO-2EY aerogel and RGO@15%EGR-2EY aerogel under visible light irradiation (E).

great promise for application to solar energy conversion due to its high conductivity, efficient visible-light-driven photoactivity, operation convenience and facile regenerability.

To further understand the significant role of improved electrical conductivity of RGO@EGR hybrid aerogel on enhancing the lifetime of electron-hole pairs and promoting photocatalytic activity of RGO@EGR-EY aerogel composites, the photoelectrochemical experiments have been performed. Fig. 4A shows the transient photocurrent response of the RGO-2EY aerogel and RGO@15%EGR-2EY aerogel. Under visible light irradiation, the photocurrent transient response for RGO@15%EGR-2EY aerogel is much higher than that for RGO-2EY aerogel, demonstrating the more efficient separation of photogenerated charge carriers over RGO@15%EGR-2EY aerogel [45,48]. Moreover, a photocurrent decay can be observed upon light irradiation, which is ascribed to the consumption of the organic dye EY under visible light irradiation [38]. To gain insight into the charge transfer process on the electrode and at the contact interface between electrode and electrolyte, the electrochemical impedance spectroscopy (EIS) Nyquist plots of the two samples have been measured. As displayed in Fig. 4B, it can be evidently seen that the Nyquist diagram of RGO@15%EGR-2EY aerogel electrode possesses more depressed semicircle at high frequency than that of RGO-2EY aerogel electrode, confirming that the successful EGR doping in RGO aerogel decrease the charge transfer resistance of hybrid aerogel system, which further confirms the result of electrical conductivity measurement [11,54]. Fig. 4C shows the cyclic voltammograms (CV) of RGO-2EY aerogel and RGO@15%EGR-2EY aerogel with obvious anodic and cathodic peaks for each sample. Since the preparation of the electrodes and electrolyte are identical for the CV curve measurement, the current density of the electrodes is related to the electron transfer rate of the electrode materials [55,56]. The fact that the current density obtained over the RGO@15%EGR-2EY aerogel electrodes is larger than that over RGO-2EY aerogel indicates the important acceleration effect of RGO@15%EGR on promoting the separation of electron-hole pairs generated from photoexcitation of EY under light irradiation. Furthermore, the photoluminescence (PL) spectrum, which is often employed to study surface processes involving the photoexcited electron transfer and recombination has also been

performed [34,57]. As depicted in Fig. 4D, it can be seen that both RGO-2EY aerogel and RGO@15%EGR-2EY aerogel show PL signals with similar curves. Notably, the PL intensity of the RGO@15%EGR-2EY aerogel obviously diminishes as compared to RGO-2EY aerogel, suggesting that the use of RGO@15%EGR with superior conductivity is able to more effectively retard the recombination of photogenerated electron-hole pairs in such aerogel composite photocatalysts [57,58].

Fig. S10A and B shows the nitrogen adsorption-desorption isotherm results of RGO-2EY aerogel and RGO@15%EGR-2EY aerogel. It can be seen that the RGO-2EY aerogel and RGO@15%EGR-2EY aerogel have similar Brunauer-Emmett-Teller (BET) surface area. In addition, the adsorption experiment for Cr(VI) in the solution in Fig. S10C shows that the RGO-2EY aerogel and RGO@15%EGR-2EY aerogel exhibit analogous adsorption ability. Therefore, it can be inferred that the surface area is not the primary reason accounting for the photoactivity difference between RGO-2EY aerogel and RGO@15%EGR-2EY aerogel. It is the different separation and transfer efficiency of photogenerated charge carriers caused by the difference of electric conductivity between RGO aerogel and RGO@15%EGR aerogel that are the key and predominant factors determining the photoactivity difference between RGO-2EY aerogel and RGO@15%EGR-2EY aerogel. Based on the above analyses, a possible reaction process of photocatalytic reduction of Cr(VI) in aqueous solution has been proposed in Fig. 4E. Under visible light irradiation, the EY absorbs visible light to form singlet excited state EY^{1*} , and then produces the lowest-lying triplet excited state EY^{3*} via an intersystem crossing (ISC) [59,60]. Subsequently EY^{3*} is reductively quenched by the sacrificial donor TEOA to simultaneously produce EY^- and $TEOA^+$ [60]. The electrons of EY^- species are transferred to the surface of graphene aerogel, which leads to the spatial separation of photogenerated charge carriers. After losing the electron, EY^- changes back to EY and the electrons on the surface of graphene aerogel can drive the photocatalytic reduction of Cr(VI) [38,61]. EGR plays two possible roles in the RGO@EGR-2EY hybrid aerogel photocatalyst system, one of which is as an electron reservoir to directly trap electrons emitted from EY upon light irradiation. Because of the superior electrical conductivity of EGR sheet than that of the RGO sheet, it can provide a longer mean free path for photoexcited electrons

to diffuse farther, and thus more effective separation of electron-hole pairs can be achieved in RGO@EGR-2EY composite aerogels [39]. The other role of EGR is acting as a “bridge” to connect the defects of RGO sheet and thus accelerates the transmission of photogenerated electrons, which is similar to the role of carbon nanotube (CNT) played in the RGO-CNT hybrid system [41,62,63]. In other words, the doping of EGR significantly leads to improved electrical conductivity of RGO@EGR-EY aerogel as compared to RGO-EY aerogel, which efficiently boosts the separation and transfer of photogenerated charge carriers and thus results in the higher photoactivity of RGO@EGR-EY hybrid aerogel than that of RGO-EY aerogel.

4. Conclusion

In summary, a series of metal-free EGR doped RGO-Eosin Y (RGO@EGR-EY) aerogel composites with enhanced electrical conductivity have been successfully synthesized by a facile one-step wet-chemistry synthesis process, during which GO acting as surfactant has been employed to disperse EGR. Because GO would be converted to RGO in the final composite without introducing any unwanted impurity, taking GO as a surfactant to disperse EGR is able to generate a clean, electrically addressable carbon–carbon interfaces. The doping of EGR with superior electrical conductivity effectively promotes the separation and transfer of charge carriers in such aerogel composite photocatalyst system, which consequently results in the much higher photoactivity of the RGO@EGR-EY aerogel than RGO-EY aerogel under identical reaction conditions. It is hoped that this work could enrich the facile fabrication of high-performance graphene aerogel-based photocatalysts via rational utilization of the highly conductive commercial graphene for practical photoredox applications.

Acknowledgments

The support from the National Natural Science Foundation of China (U1463204, 20903023 and 21173045), the Award Program for Minjiang Scholar Professorship, the Natural Science Foundation (NSF) of Fujian Province for Distinguished Young Investigator Rolling Grant (2017J07002), the Independent Research Project of State Key Laboratory of Photocatalysis on Energy and Environment (NO. 2014A05), the 1 st Program of Fujian Province for Top Creative Young Talents, and the Program for Returned High-Level Overseas Chinese Scholars of Fujian province is gratefully acknowledged.

Appendix A. Supplementary data

Supplementary data associated with this article can be found, in the online version, at <https://doi.org/10.1016/j.apcatb.2017.12.032>.

References

- [1] N. Zhang, M.-Q. Yang, S. Liu, Y. Sun, Y.-J. Xu, Chem. Rev. 115 (2015) 10307–10377.
- [2] M.-Q. Yang, N. Zhang, M. Pagliaro, Y.-J. Xu, Chem. Soc. Rev. 43 (2014) 8240–8254.
- [3] W. Han, L. Ren, L. Gong, X. Qi, Y. Liu, L. Yang, X. Wei, J. Zhong, ACS Sustain. Chem. Eng. 2 (2014) 741–748.
- [4] C. Mu, Y. Zhang, W. Cui, Y. Liang, Y. Zhu, Appl. Catal. B 212 (2017) 41–49.
- [5] G. Palmissano, V. Augugliaro, M. Pagliaro, L. Palmissano, Chem. Commun. (2007) 3425–3437.
- [6] C. Han, N. Zhang, Y.-J. Xu, Nano Today 11 (2016) 351–372.
- [7] Y. Li, W. Cui, L. Liu, R. Zong, W. Yao, Y. Liang, Y. Zhu, Appl. Catal. B 199 (2016) 412–423.
- [8] C. Li, G. Shi, Nanoscale 4 (2012) 5549–5563.
- [9] W. Jiang, Y. Zhu, G. Zhu, Z. Zhang, X. Chen, W. Yao, J. Mater. Chem. A 5 (2017) 5661–5679.
- [10] W. Wan, S. Yu, F. Dong, Q. Zhang, Y. Zhou, J. Mater. Chem. A 4 (2016) 7823–7829.
- [11] B. Qiu, M. Xing, J. Zhang, J. Am. Chem. Soc. 136 (2014) 5852–5855.
- [12] X. Cao, Z. Yin, H. Zhang, Energy Environ. Sci. 7 (2014) 1850–1865.
- [13] D.R. Dreyer, S. Park, C.W. Bielawski, R.S. Ruoff, Chem. Soc. Rev. 39 (2010) 228–240.
- [14] J. Luo, L.J. Cote, V.C. Tung, A.T.L. Tan, P.E. Goins, J. Wu, J. Huang, J. Am. Chem. Soc. 132 (2010) 17667–17669.
- [15] X. Li, J. Yu, S. Wagh, A.A. Al-Ghamdi, J. Xie, Small 12 (2016) 6640–6696.
- [16] Y. Zhang, N. Zhang, Z.-R. Tang, Y.-J. Xu, Phys. Chem. Chem. Phys. 14 (2012) 9167–9175.
- [17] S. Liu, B. Weng, Z.-R. Tang, Y.-J. Xu, Nanoscale 7 (2015) 861–866.
- [18] R. Ciriminna, N. Zhang, M.-Q. Yang, F. Meneguzzo, Y.-J. Xu, M. Pagliaro, Chem. Commun. 51 (2015) 7090–7095.
- [19] K.R. Paton, E. Varlla, C. Backes, R.J. Smith, U. Khan, A. O'Neill, C. Boland, M. Lotya, O.M. Istrate, P. King, Nat. Mater. 13 (2014) 624–630.
- [20] Y. Hernandez, V. Nicolosi, M. Lotya, F.M. Blighe, Z. Sun, S. De, I.T. McGovern, B. Holland, M. Byrne, Y.K. Gun'ko, J.J. Boland, P. Niraj, G. Duesberg, S. Krishnamurthy, R. Goodhue, J. Hutchison, V. Scardaci, A.C. Ferrari, J.N. Coleman, Nat. Nanotechnol. 3 (2008) 563–568.
- [21] Y.L. Zhong, Z. Tian, G.P. Simon, D. Li, Mater. Today 18 (2015) 73–78.
- [22] J.N. Coleman, Acc. Chem. Res. 46 (2013) 14–22.
- [23] D. Li, M.B. Muller, S. Gilje, R.B. Kaner, G.G. Wallace, Nat. Nanotechnol. 3 (2008) 101–105.
- [24] Y.T. Liang, M.C. Hersam, J. Am. Chem. Soc. 132 (2010) 17661–17663.
- [25] S. Stankovich, R.D. Piner, X. Chen, N. Wu, S.T. Nguyen, R.S. Ruoff, J. Mater. Chem. 16 (2006) 155–158.
- [26] V.C. Tung, J.-H. Huang, J. Kim, A.J. Smith, C.-W. Chu, J. Huang, Energy Environ. Sci. 5 (2012) 7810–7818.
- [27] H. Wang, S. Lu, Y. Zhang, F. Lan, X. Lu, Y. Xiang, J. Mater. Chem. A 3 (2015) 6282–6285.
- [28] Y. Liang, D. Wu, X. Feng, K. Müllen, Adv. Mater. 21 (2009) 1679–1683.
- [29] F. Kim, L.J. Cote, J. Huang, Adv. Mater. 22 (2010) 1954–1958.
- [30] J. Kim, L.J. Cote, F. Kim, W. Yuan, K.R. Shull, J. Huang, J. Am. Chem. Soc. 132 (2010) 8180–8186.
- [31] V.C. Tung, J.-H. Huang, I. Tevis, F. Kim, J. Kim, C.-W. Chu, S.I. Stupp, J. Huang, J. Am. Chem. Soc. 133 (2011) 4940–4947.
- [32] L.J. Cote, F. Kim, J. Huang, J. Am. Chem. Soc. 131 (2009) 1043–1049.
- [33] D.W. Boukhvalov, M.I. Katsnelson, J. Am. Chem. Soc. 130 (2008) 10697–10701.
- [34] Y. Zhang, Z.-R. Tang, X. Fu, Y.-J. Xu, ACS Nano 4 (2010) 7303–7314.
- [35] Y. Zhang, Z.-R. Tang, X. Fu, Y.-J. Xu, ACS Nano 5 (2011) 7426–7435.
- [36] N. Zhang, M.-Q. Yang, Z.-R. Tang, Y.-J. Xu, ACS Nano 8 (2014) 623–633.
- [37] W.S. Hummers, R.E. Offeman, J. Am. Chem. Soc. 80 (1958) 1339–1339.
- [38] M.-Q. Yang, N. Zhang, Y. Wang, Y.-J. Xu, J. Catal. 346 (2017) 21–29.
- [39] Y.T. Liang, B.K. Vijayan, K.A. Gray, M.C. Hersam, Nano Lett. 11 (2011) 2865–2870.
- [40] Y. Zhang, N. Zhang, Z.-R. Tang, Y.-J. Xu, J. Phys. Chem. C 118 (2014) 5299–5308.
- [41] X. Lu, H. Dou, B. Gao, C. Yuan, S. Yang, L. Hao, L. Shen, X. Zhang, Electrochim. Acta 56 (2011) 5115–5121.
- [42] J. Kim, L.J. Cote, J. Huang, Acc. Chem. Res. 45 (2012) 1356–1364.
- [43] J.M. Lee, E.K. Mok, S. Lee, N.S. Lee, L. Debbichi, H. Kim, S.J. Hwang, Angew. Chem. Int. Ed. 55 (2016) 8546–8550.
- [44] S. Zinadini, A.A. Zinatizadeh, M. Rahimi, V. Vatanpour, H. Zangeneh, J. Membr. Sci. 453 (2014) 292–301.
- [45] M.-Q. Yang, C. Han, N. Zhang, Y.-J. Xu, Nanoscale 7 (2015) 18062–18070.
- [46] S. Stankovich, D.A. Dikin, R.D. Piner, K.A. Kohlhaas, A. Kleinhammes, Y. Jia, Y. Wu, S.T. Nguyen, R.S. Ruoff, Carbon 45 (2007) 1558–1565.
- [47] N. Zhang, M.-Q. Yang, Z.-R. Tang, Y.-J. Xu, J. Catal. 303 (2013) 60–69.
- [48] F.-X. Xiao, J. Miao, B. Liu, J. Am. Chem. Soc. 136 (2014) 1559–1569.
- [49] K.-Q. Lu, Q. Quan, N. Zhang, Y.-J. Xu, J. Energy Chem. 25 (2016) 927–935.
- [50] Y. Fan, W. Ma, D. Han, S. Gan, X. Dong, L. Niu, Adv. Mater. 27 (2015) 3767–3773.
- [51] X. Song, Y. Chen, M. Rong, Z. Xie, T. Zhao, Y. Wang, X. Chen, O.S. Wolfbeis, Angew. Chem. Int. Ed. 55 (2016) 3936–3941.
- [52] Q. Li, Z. Jin, Z. Peng, Y. Li, S. Li, G. Lu, J. Phys. Chem. C 111 (2007) 8237–8241.
- [53] R. Abe, K. Hara, K. Sayama, K. Domen, H. Arakawa, J. Photochem. Photobiol. A: Chem. 137 (2000) 63–69.
- [54] D. Wang, D. Choi, J. Li, Z. Yang, Z. Nie, R. Kou, D. Hu, C. Wang, L.V. Saraf, J. Zhang, I.A. Aksay, J. Liu, ACS Nano 3 (2009) 907–914.
- [55] X. Pan, Y. Zhao, S. Liu, C.L. Korzeniewski, S. Wang, Z. Fan, ACS Appl. Mater. Interfaces 4 (2012) 3944–3950.
- [56] B. Weng, Q. Quan, Y.-J. Xu, J. Mater. Chem. A 4 (2016) 18366–18377.
- [57] Z. Mou, Y. Dong, S. Li, Y. Du, X. Wang, P. Yang, S. Wang, Int. J. Hydrg. Energy 36 (2011) 8885–8893.
- [58] X. Yu, R. Du, B. Li, Y. Zhang, H. Liu, J. Qu, X. An, Appl. Catal. B 182 (2016) 504–512.
- [59] W. Zhang, C. Kong, W. Gao, G. Lu, Chem. Commun. 52 (2016) 3038–3041.
- [60] L. Yang, J. Huang, L. Shi, L. Cao, W. Zhou, K. Chang, X. Meng, G. Liu, Y. Jie, J. Ye, Nano Energy 36 (2017) 331–340.
- [61] Z. Li, B. Tian, W. Zhang, X. Zhang, Y. Wu, G. Lu, Appl. Catal. B 204 (2017) 33–42.
- [62] L. Qiu, X. Yang, X. Gou, W. Yang, Z.-F. Ma, G.G. Wallace, D. Li, Chem. Eur. J. 16 (2010) 10653–10658.
- [63] Z. Sui, Q. Meng, X. Zhang, R. Ma, B. Cao, J. Mater. Chem. 22 (2012) 8767–8771.